PCCP

Accepted Manuscript

ROYAL SOCIETY OF CHEMISTRY

www.rsc.org/pccp

Journal Name

ARTICLE

Synthesis of magnetofluorescence Gd-doped $CuInS_2$/ZnS quantum dots with enhanced longitudinal relaxivity

Received 00th January 20xx,
Accepted 00th January 20xx

DOI: 10.1039/x0xx00000x

www.rsc.org/

Jia-Yaw Chang,* Guan-Rong Chen, Jyun-Dong Li

In this paper, we describe the rapid microwave-assisted synthesis of Gd^{3+}-doped $CuInS_2$ (Gd:CIS) quaternary quantum dots (*q*-dots), which integrate functions of optical fluorescence and magnetic resonance imaging. Through passivation of ZnS shells around Gd:CIS cores, high-quality and robust photostable Gd:CIS/ZnS core/shell *q*-dots with enhanced quantum yields were obtained. The intensity and peak-to-peak linewidth of the electron spin resonance (EPR) signal was found to vary depending on the Gd^{3+} concentration of Gd:CIS/ZnS. Benefiting from the incorporation of paramagnetic Gd^{3+} ions, the formed *q*-dots exhibited well-resolved and strong signals of electron paramagnetic resonance and provided significant contrast enhancement in T1-weighted images owing to the remarkably high longitudinal relaxivity (r_1 = 55.90 mM^{-1} s^{-1}) and low r_2/r_1 ratio (1.42), which is significantly higher than those of commercially available T_1 contrast agents. We expect that this facile one-pot synthetic strategy can be extended to the preparation of other Cu-based sulfide quaternary nanomaterals.

1. Introduction

Recently, the design and synthesis of dual-modal imaging probes based on magnetic resonance (MR) and optical imaging modalities has gradually gained popularity because of their ability to integrate the benefits of each imaging modality while compensating for the weaknesses inherent in each imaging method. For example, MR imaging is a powerful non-invasive diagnostic imaging technique for disease diagnosis because of its high spatial resolution, deep tissue penetration, and tomographic capabilities; however, it is not as sensitive as optical imaging, and it is difficult to visualize biological processes *in vitro* and *in vivo*. Optical imaging has excellent sensitivity for quantifying molecular events at subcellular levels, but it suffers from low tissue penetration.

Among available nanomaterials, colloidal semiconductor nanocrystals with radii smaller than the Bohr exciton radius, known as quantum dots (QDs), have attracted extensive interest among scientists in many research fields such as biological tags, light-emitting diodes, lasers, and photovoltaic devices. In particular, several unique photophysical properties over organic fluorophores, such as strong photoluminescence, high extinction coefficients, excellent photostability, long fluorescence lifetime, the adjustable emission spectra, multicolor emission with a single-wavelength excitation, make them particularly appealing for luminescence tagging, biological imaging, and medical diagnostics. Much effort has been focused on the use of cadmium chalcogenide QDs for simultaneous imaging and therapeutic applications.[1–4] However, cadmium chalcogenide QDs are toxic to biological systems, which has brought much attention to their potential adverse effects on the environment and on human health, limiting their validation in large-scale clinical studies.

In recent years, the synthesis of I–III–VI semiconductor nanoparticles such as $CuInS_2$ has received a great deal of attention because they not only have attractive optical and electronic properties, they also do not have toxic heavy metal ions (e.g. cadmium, lead, and mercury).[5–7] However, these QDs were often fabricated by an organic phase approach, which requires a high reaction temperature to decompose the precursors and hydrophobic capping ligands to prevent aggregation. For biological applications, these hydrophobic QDs often need further modification; therefore, complicated processes, including ligand exchange, silica layer coating, and amphiphilic polymer encapsulation, are needed in order to transfer these hydrophobic QDs into aqueous solvents.[8–10] These additional procedures during modification usually result in adverse effects, such as a reduction of emission performance, weaker water solubility, and colloidal instability when dispersed in aqueous phase.[11] As compared to organic synthesis, direct aqueous synthesis of QDs can be performed under mild conditions in a process that is simple and reproducible with less energy consumption.

Department of Chemical Engineering, National Taiwan University of Science and Technology, 43, Section 4, Keelung Road, Taipei, 10607, Taiwan, Republic of China
E-mail: jychang@mail.ntust.edu.tw

† *Footnotes relating to the title and/or authors should appear here.*
Electronic Supplementary Information (ESI) available: [details of any supplementary information available should be included here]. See DOI: 10.1039/x0xx00000x

Recently, several groups reported the synthesis of $CuInS_2$ ternary QDs (*t*-dots) with superior water solubility and favorable biocompatibility; nevertheless, several issues remain in aqueous synthetic routes, such as relatively long reaction times and low quantum yield (QY).[12–15] Moreover, to the best of our knowledge, little work on the direct aqueous synthesis of high-quality Cu-based sulfide quaternary QDs (*q*-dots) has been carried out because of the large solubility differences of multiple precursors in conventional aqueous synthesis routes.

In this study, we developed a convenient means for the preparation of aqueous-phase gadolinium (Gd^{3+})-doped $CuInS_2$ (Gd:CIS) *q*-dots under microwave irradiation in approximately 10 min. Incorporation of paramagnetic Gd^{3+} into a $CuInS_2$ host lattice made it effective as a T_1 contrast agent because Gd^{3+} ions have seven unpaired electrons in its 4f orbitals ($4f^7$), which gives the strongest T_1 contrast effect compared to other paramagnetic ions such as Mn^{2+} (five unpaired electrons), Co^{2+} (three unpaired electrons), and Eu^{3+} (six unpaired electrons). To our knowledge, this is the first reported direct synthesis of Gd:CIS *q*-dots in aqueous phase. The optimal synthetic conditions for obtaining Gd:CIS *q*-dots with good optical properties are described in detail. Through ZnS passivation, the resulting Gd:CIS/ZnS core/shell *q*-dots exhibited strong photoluminescence, robust photostability, high longitudinal relaxivity, and low r_2/r_1 ratio, imparting the potential for optical/MR imaging.

2. Experimental

2.1 Materials

Thiourea (CH_4N_2S, 99%) was purchased from Alfa-Aesar (Ward Hill, USA). Copper(I) chloride dihydrate ($CuCl_2{\cdot}2H_2O$, 99.99%), glutathione (GSH, 98%), and citric acid trisodium salt (SC, 98%) were purchased from Sigma-Aldrich (Milwaukee, USA). Indium(III) chloride ($InCl_3$, 99.99%), Sodium sulfide nonahydrate ($Na_2S{\cdot}9H_2O$, 98%), gadolinium(III) chloride ($GdCl_3$, 99.99%) were purchased from Acros Organics (New Jersey, USA). Zinc acetate ($Zn(OAc)_2$, 99%) was obtained from J. T. Baker (Phillipsburg, USA).

2.2 Synthesis of Gd:CIS core and Gd:CIS/ZnS core/shell *q*-dots

The synthetic process was conducted using a single-mode microwave reactor (Anton Paar Monowave 300) operating at 850 W magnetron output power. For obtaining Gd:CIS core *q*-dots with high optical performance, we studied various synthetic conditions in the original solution while keeping the other experimental variables fixed. The synthetic conditions included temperature (from 130 to 220 °C), pH (from 4.0 to 8.0), and reactant molar ratios [Cu:In (from 1:3 to 1:8), Cu:SC (from 1:8 to 1:18), and Cu:GSH (from 1/4 to 1/20)].

The optimal reaction conditions of the Gd:CIS core *q*-dots were identified as follows: The concentration of $CuCl_2$ was set as 2 mM, and the feed molar ratios of Cu:Gd:In:GSH:SC were 1:1:6:4:16. In a typical synthesis, $CuCl_2$, $InCl_3$, and $GdCl_3$ were dissolved in 15 mL of deionized water containing GSH and SC and loaded into a 30 mL vessel. Subsequently, 0.8 mL of a Na_2S (0.16 mmol) aqueous solution was quickly added. The Na_2S stock solution was prepared by dissolving 0.4804 g Na_2S in 10 mL of water. The pH value of the reaction mixture was adjusted to 5.0 by the dropwise addition of a 1.0 M NaOH solution. The solution was subsequently heated with microwave irradiation to a reaction temperature of 220 °C for 10 min.

For the preparation of the Gd:CIS/ZnS core/shell *q*-dots, 4 mL of a ZnS precursor solution was delivered into the above solution containing Gd:CIS core *q*-dots. ZnS precursor solution was obtained by mixing 0.8 mmol $Zn(OAc)_2$, 1.2 mmol GSH, and 2.4 mmol thiourea. The pH was adjusted to 6.0 by dropwise addition of 1 M NaOH. The mixture was further irradiated in a microwave reactor at 90 °C for 30 min to allow overcoating by the ZnS shells. Upon completion, the reaction was cooled to room temperature using forced-air cooling to yield Gd:CIS/ZnS core/shell *q*-dots. The resulting *q*-dots were filtered and then isolated with 2-propanol via centrifugation at 6000 rpm for 25 min.

2.3 Material characterization

Transmission electron microscopy (TEM), high-resolution transmission electron microscopy (HR-TEM) images, and energy dispersive X-ray spectroscopy (EDS) of the samples were taken at 200 kV with a FEI Tecnai G2 F20 microscope (Philips, Holland). The X-ray powder diffraction (XRD) patternswere recorded using a Bruker D8 Discover X-ray Diffractometer (German), equipped with high-intensity Cu $K_{\alpha1}$ irradiation (λ = 1.5406 Å). The Gd concentration of the samples was determined by inductively coupled plasma atomic emission spectroscopy (ICP-AES) (Y 2000−2, JobinYvon Horiba). The relaxivity and MR images were performed in a 7 T BioSpec 70/30 scanner (70/30 BrukerBioSpin; Ettlingen, Germany) equipped with actively shielded gradient coils. The parameters for T1 measurements were set as follows: echo time (TE) = 10 ms; repetition time (TR) = 11000 ms. Electron spin resonance (EPR) spectra were collected at room temperature on a BrukerElexsys E-580 system.

2.4 Optical characterization

UV–visible spectrophotometer (JASCO V-630) and fluorescence spectrophotometer (JASCO FP-6500) were utilized to record the optical absorption and emission spectra of the as-prepared samples, respectively. Two-dimensional photoluminescence excitation spectroscopy (2D-PLE) photostability test were recorded on a Fluorolog-3 spectrofluorometer (HORIBA JobinYvon, Japan) equipped with a 450 W xenon light. Photoluminescence decay dynamics was performed using a Jobin-Yvon H10 monochromator equipped with a pulsed diode laser (PDL 200-B, 450 nm, PicoQuant) and a PMA 185 photomultipier tube (PicoQuant) with a resolution of 30 ps. Photon counting was performed using a Model NanoHarp 250 multichannel scaler (PicoQuant). The time-resolved emission signals were analyzed using the FluoFit program (PicoQuant, GmbH) to extract lifetime values, while the fitting quality was evaluated by the weighed residuals' autocorrelation function (random distribution of small values) and reduced chi-square ($\chi^2 \leq 1.0$). Photoluminescence quantum

yields (Φ) were measured by comparing the integrated emission of the *q*-dots in water with that of a fluorescent dye (Rhodamine 6G, Φ_{R6G}= 95% in methanol) and using data derived from the luminescence and the absorption spectra, as follows:

$$\Phi_{sample} = \Phi_{R6G} \times \left(\frac{1-10^{-a_{R6G}}}{1-10^{-a_{sample}}}\right) \times \left(\frac{I_{sample}}{I_{R6G}}\right) \times \left(\frac{\varepsilon_{sample}}{\varepsilon_{R6G}}\right)^2 \quad (1)$$

where subscript sample and R6G represented the as-synthesized *q*-dots and Rhodamine 6G, respectively; α was optical density values at the excitation wavelength were set the same in the range of 0.02–0.05, *I* was the integrated area of emission spectra, ε was the refractive index of the solvent used.

3. Results and discussion

Herein, we employed $CuInS_2$ *t*-dots as the host matrix for the incorporation of the Gd^{3+} dopant. The synthetic technique was a nucleation-doping strategy, which was achieved via simultaneous introduction of both dopant and host ions into a reaction system and subsequent heating at the desired temperature. Starting from $CuInS_2$ *t*-dots synthesized by the protocol of Chen et al.,[15] we employed hydrothermal synthesis of Gd:CIS *q*-dots using $GdCl_3$ as the dopant, $CuCl_2$ and $InCl_3$ as cationic precursors, Na_2S as a sulfur source, and water as a solvent in the presence of dual stabilizers (GSH and SC) by using microwave irradiation instead of conventional heating (Scheme 1). As compared to conventional heating techniques, microwave irradiation has proven to be an excellent technique for synthesizing QDs owing to several distinct and fascinating features, including environmentally friendliness, low energy of consumption, and easy control of the temperature and pressure profile. In particular, microwave-irradiation heating was utilized in the synthesis to initiate rapid homogeneous nucleation of multiple components and to reduce the crystallization time, which narrowed the size distribution and improved the crystallinity of the QDs.

Scheme 1. Schematic of the formation of Gd:CIS core and Gd:CIS/ZnS core/shell *q*-dots under microwave irradiation.

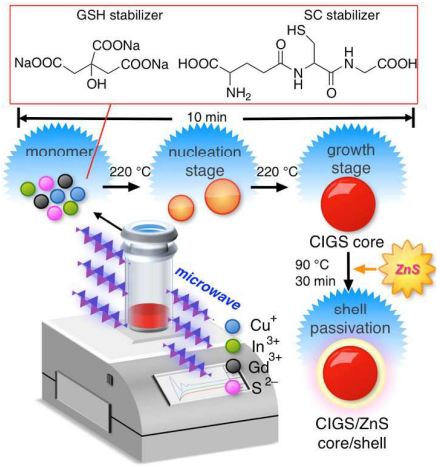

3.1 Influence of reaction time and temperature

The temporal evolution of the absorption and the photoluminescence (PL) spectra of Gd:CIS *q*-dots prepared at a Cu:In:Gd precursor ratio of 1:6:1 at a reaction temperature of 140 °C are presented in Figure 1a. There is an obvious gradual redshift of the absorption and emission peaks with increasing reaction time, together with a gradual decrease of the PL intensity under microwave irradiation. This red shift of the optical properties can be mainly regarded as the effect of weak quantum confinement with

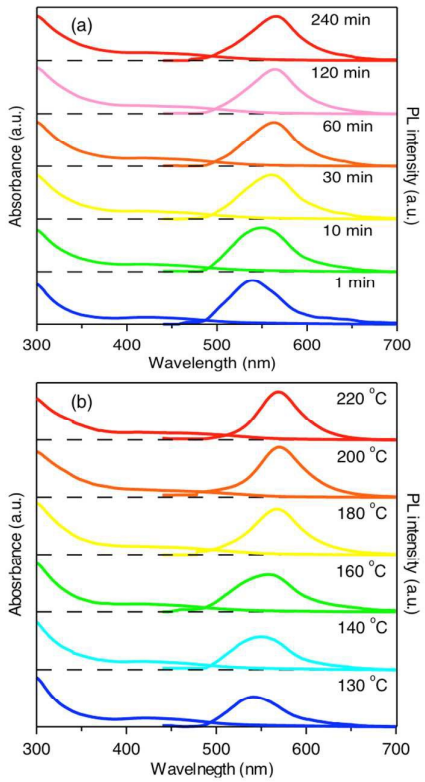

Figure 1. (a) Temporal evolution of the optical absorption and PL emission spectra of Gd:CIS *q*-dots grown at 140 °C. (b) The absorption and PL spectra of Gd:CIS *q*-dots prepared at different heating temperatures for 10 min. Experimental conditions: the precursor concentration of Cu is 2 mM and [Cu]:[In]:[Gd]:[SC]:[GSH] = 1:6:1:16:12

increasing particle size.

To investigate the role of temperature, Gd:CIS *q*-dots were prepared under identical conditions ([Cu] = 2 mM, molar ratio of Cu:In:Gd at 1:6:1) but heated at different temperatures from 130 to 220 °C for 10 min. As the reaction temperature increased, both the absorption edge, the PL peak position shifted to longer wavelengths systematically (Figure 1b), and the full width at half-maximum (FWHM) became narrower. For example, in comparison to the sample prepared at 140 °C (λ = 550 nm, FWHM = 73 nm), the emission spectrum of the Gd:CIS *q*-dots at 220 °C appears symmetric, with a narrow emission peak (λ = 570 nm, FWHM = 54 nm). The increased temperature not only enhanced the thermolysis rate of the precursors, it

also promoted the reaction mobility of the ligand and precursors, thus increasing the nucleation and growth rates of *q*-dots, which resulted in the redshift in absorption and emission, accompanied by a narrow particle-size distribution and enhanced PL QY. This phenomenon, mainly attributed to the growth rate of the *q*-dots, was accompanied by an increase of temperature, leading to the size increase of the *q*-dots. It is broadly accepted that the aqueous synthetic conditions achieved under normal pressure and a reaction temperature below 100 °C, which reduces the reaction rate, results in abundant surface defects and poor optical performance of the QDs. On the other hand, the microwave-assisted synthetic method allows for a higher reaction temperature, which accelerates the reaction rate, resulting in better crystallinity and enhanced emission of the QDs.

3.2 Influence of feed molar ratios of reactants and pH values

The PL performance of the Gd:CIS *q*-dots was also varied by altering the pH values and reactant molar ratios (the Cu:In, Cu:SC, and Cu:GSH precursor ratios) of the original solution while keeping the same reaction time of 10 min at 220 °C, as shown in Figure 2. With decreasing Cu:In molar fraction, the emission intensity increased remarkably and approached the maximum intensity at a Cu:In ratio of 1:6, as illustrated in Figure 2a. The increase of emission intensity can be ascribed to $CuInS_2$ semiconductors expressing a defect/vacancy-related emission instead of an excitonic emission. In general, chalcopyrite $CuInS_2$ reportedly possesses tremendous structural tolerance for off-stoichiometric variations; as a result, it tends to exhibit various defects. Cu vacancies are preferably generated because of weaker Cu–S bonds, which promote a large number of copper vacancies and induce antisite defects in the lattice.[16] Therefore, a certain amount of excessive In^{3+} could substitute for Cu^{+}, thus inhibiting the generation of vacancies. Several reports have determined that indium-rich $CuInS_2$ *t*-dots of high emission QYs are often synthesized by adopting an excess of In reactants relative to Cu reactants.[16–18] A similar feature is also seen in CdTe semiconductors that have intrinsic defects (Cd vacancies) inside the crystal.[19] It has been shown that $Cd_xZn_{1-x}Te$ QDs with high PL QYs can be prepared by incorporating Zn into CdTe, which is explained in terms of Cd vacancy sites occupied by additional Zn ions, leading to the minimization of nonradiative emission centers and high emission intensities.[20] Nevertheless, as the In molar fraction increases, In-related intrinsic defects of *q*-dots may accumulate to a relatively high concentration. Therefore, too high a molar fraction of In precursors in the reaction mixture becomes unfavorable to acquiring high-quality Gd:CIS *q*-dots, which decreases the PL intensity.

The effect of the Cu:SC and Cu:GSH molar ratios on the PL performance of the Gd:CIS *q*-dots are illustrated in Figures 2b and 2c. We varied the Cu:SC molar ratio from 1:8 to 1:18 while keeping the other experimental variables fixed. The resulting PL performance of the Gd:CIS *q*-dots reached a maximum intensity at a Cu:SC molar ratio of 1:16, and then it declined with

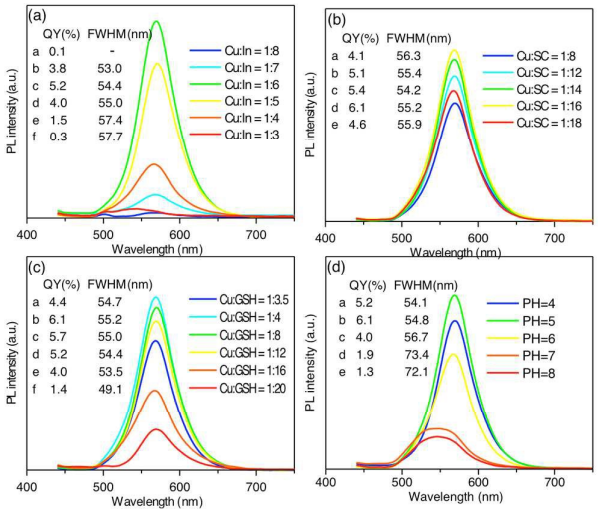

Figure 2. Fluorescence emission spectra of Gd:CIS *q*-dots prepared under different (a) Cu:In, (b) Cu:SC, and (c) Cu:GSH molar ratios, keeping the other variables constant as follows: the precursor concentration of Cu is 2 mM and (a) [Cu]:[Gd]:[SC]:[GSH] = 1:1:16:12. (b) [Cu]:[In]:[Gd]:[GSH] = 1:6:1:4. (c) [Cu]:[In]:[Gd]:[SC] = 1:6:1:16. The pH values were all set at 5.0. (d) Fluorescence emission spectra of Gd:CIS *q*-dots prepared by using different pH values of the growth solution from 4.0 to 8.0. Experimental conditions in (d): the precursor concentration of Cu is 2 mM and [Cu]:[In]:[Gd]:[SC]:[GSH] = 1:6:1:16:4. The reaction time and temperature were fixed to 10 min and 220 °C, respectively, for all cases.

increasing SC feed molar ratios, as shown in Figure 2b. Upon changing the mole fraction ratio of Cu:GSH from 1:4 to 1:20, the emission intensities of Gd:CIS *q*-dots gradually decreased as the feed ratio of GSH increased (Figure 2c). When the ratio of GSH to Cu was 4, Gd:CIS *q*-dots with the highest emission intensity were obtained.

Furthermore, we also compared the PL properties of Gd:CIS *q*-dots obtained at different starting pH values. Figure 2d displays the PL spectra of Gd:CIS *q*-dots prepared at pH values from 4.0 to 8.0. The good optical performance of the as-prepared Gd:CIS *q*-dots was obtained under acidic conditions. When the pH value of the cationic precursors was set at 5.0, the as-obtained Gd:CIS *q*-dots showed maximum emission and a relatively narrow FWHM, suggesting narrower particle-size distributions and good optical performance under acidic conditions. However, upon increasing the pH value of the reaction system to 7.0, the emission intensity started to decrease and the FWHM became broader. Moreover, a shift in the emission peak toward a shorter wavelength was observed with increasing starting pH values, indicating a slower growth rate and broader size distribution during *q*-dot formation. In Figure S1, the emission intensity of PL decreased gradually with the increase of Gd feed molar ratios. This observation might be attributed to the formation of excessive Gd defects in *q*-dots, which leads to increased probability of the nonradiative recombination.

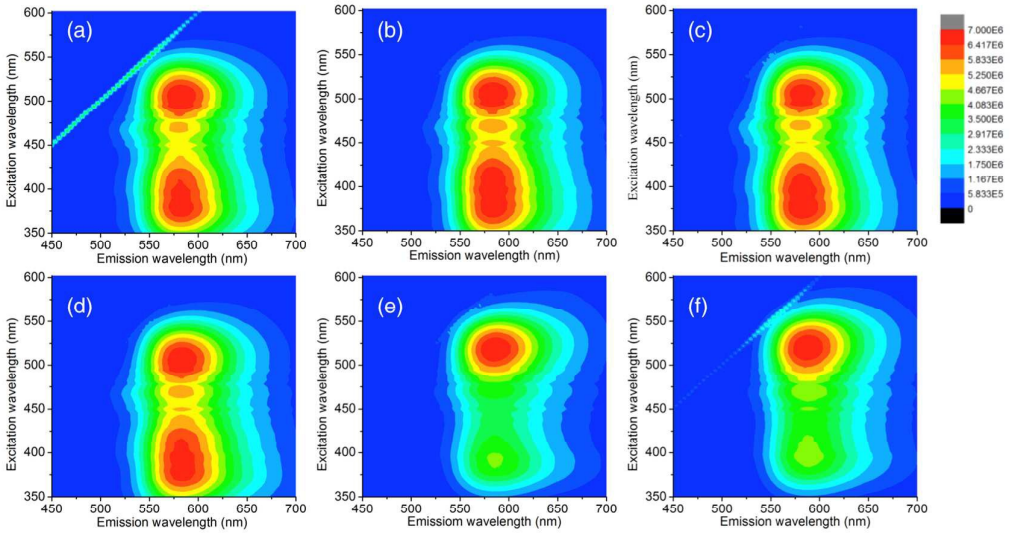

Figure 3. 2D PLE map of Gd:CIS *q*-dots prepared under different Cu/Gd molar ratios: (a) Cu:Gd = 1:0, (b) Cu:Gd = 1:0.5, (c) Cu:Gd = 1:1, (d) Cu:Gd = 1:2, (e) Cu:Gd = 1:3, and (f) Cu:Gd = 1:5, keeping the other variables constant.

To further investigate the photophysical properties of the obtained Gd:CIS *q*-dots, 2D PLE spectra were chosen for the optical characterization. The 2D PLE maps shown in Figure 3 indicate that the emission intensity changed as a function of excitation wavelength, whereas the emission peak position did not redshift or blueshift upon alterations to the excitation wavelength. It can be noticed from Figure 3 that the obtained PLE maps exhibit dual-excitation maxima, with a single emission (580 nm) for samples with Cu:Gd molar ratios from 1:0 to 1:2. For instance, the PLE maps indicate that dual-excitation maxima occurred at approximately 400 nm and 520 nm with Gd:CIS *q*-dots prepared with Cu:Gd molar ratios lower than 1:2. The energy separation between the dual-excitation maxima is estimated to be 10.3 eV. The dual-excitation signal may be related to the intrinsic properties of $CuInS_2$ materials and the exact mechanism for this observation was not clear. This result was consistent with the findings of Xiong et al. that $CuInS_2$/ZnS QDs exhibited two excitation peaks and that their intensity depended on the Cu:In ratios.[13] In addition, similar observation was reported previously in other nanomaterials, such as metal clusters[21-24] and graphene QDs[25-28].

When Cu:Gd molar ratio was at 1:0.5 and 1:2, PLE spectra of Gd:CIS *q*-dots show similar profile as seen in pristine $CuInS_2$ QDs without the incorporation of Gd^{3+} dopants. We postulate that Gd^{3+} dopants homogeneously distributed inside $CuInS_2$ host-matrix, which did not affect the internal electronic transitions of pristine materials.

However, with the increasing ratio of Cu:Gd from 1:2 to 1:3 and 1:5, the corresponding excitation spectra exhibited a single peak at approximately 510 nm, and the excitation intensity at ~400 nm gradually decreased. This is presumably due to a non-uniform Gd^{3+} doping or the aggregation of Gd^{3+} clusters affect the intrinsic properties of pristine $CuInS_2$ QDs, which is further supported by EPR spectra (seen in Figure 6).

3.3 Epitaxial growth of the ZnS shell on the Gd:CIS core

Generally, the maximum PL QY is correlated to minimal amounts of surface-trap states on the surfaces of QDs. To further improve the PL QY, a subsequent attempt to passivate the inorganic surfaces was carried out by in situ overgrowth of ZnS shells onto the core *q*-dots following the modified procedure reported in ref 15. On the basis of the experiments discussed above, the optimal reaction conditions of the Gd:CIS *q*-dots were identified as follows: The molar ratios of the precursors were Cu:Gd:In = 1:1:6 and Cu:SC:GSH = 1:16:4, with a concentration of Cu precursors of 2 mM. Gd:CIS *q*-dots showed elemental analysis results of Cu/In/Gd = 0.35/0.61/0.04 by ICP-AES. To avoid formation of additional ZnS QDs, ZnS shell deposition was carried out at 90 °C under microwave irradiation to yield Gd:CIS/ZnS core/shell structures (Scheme 1).

Figure 4a shows the absorption and PL spectra of the Gd:CIS core and the Gd:CIS/ZnS core/shell *q*-dots. The Gd:CIS/ZnS core/shell *q*-dots display a significant increase in emission intensity as compared to the Gd:CIS core *q*-dots. The maximum intensity emission spectrum of the Gd:CIS/ZnS core/shell *q*-dots is centered at 560 nm (λ_{max}), with an excitation wavelength of 430 nm. A blueshift of the maximum wavelength is found in the emission spectra of the Gd:CIS/ZnS core/shell *q*-dots as compared to the pristine Gd:CIS core *q*-dots. This PL peak shift to shorter wavelengths is considered to be the result of shrinkage of the Gd:CIS core *q*-dots as a result of partial cation exchange between the cationic ions of the core *q*-dots and the Zn ions overcoating the ZnS shells. Similar observations of blueshifts after growing ZnS on $CuInS_2$ cores were reported in an earlier study.[8] Moreover,

the PL QY of the Gd:CIS/ZnS *q*-dots was significantly enhanced by microwave irradiation to a maximal value of ~26% from the ~6% of the bare cores. The possible reason for the PL QY improvement of the core/shell *q*-dots as compared to the plain *q*-dots might be that ZnS shells with wider band gaps not only effectively diminished the number of defects or dangling bonds on the surfaces of the original core particles but also energetically reduced the leakage of excitons outside the core. The enhanced PL performance agrees well with the photoluminescence lifetime (Figure 4b) and photostability (Figure 4c) results.

Table 1. The fluorescent decay parameters of Gd:CIS core and Gd:CIS/ZnS core/shell *q*-dots.

Sample	α_1 (%)	τ_1 (ns)	α_2 (%)	τ_2 (ns)	<τ> (ns)	χ^2
Gd:CIS	84.5	518	15.5	72.0	449	1.00
Gd:CIS/ZnS	81.5	541	18.5	159	470	1.00

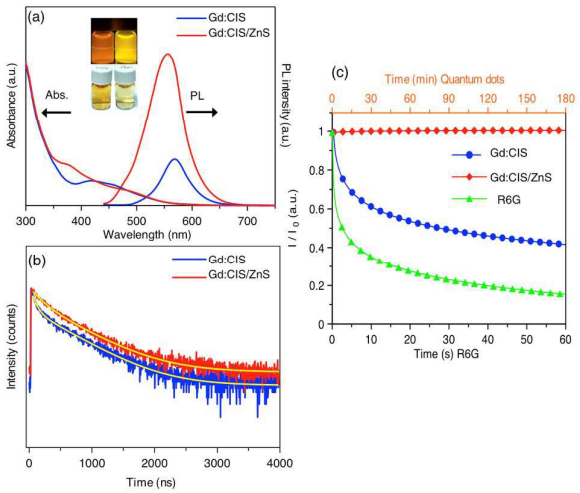

Figure 4. (a) The absorption and PL spectra of Gd:CIS core and Gd:CIS/ZnS core/shell *q*-dots. Inset displays photograph of the Gd:CIS *q*-dots without (left) and with (right) the overcoating of ZnS shells. (b) Fluorescence emission decay curves of Gd:CIS core and Gd:CIS/ZnS core/shell *q*-dots. (c) Photostability comparison of the as-prepared Gd:CIS core and Gd:CIS/ZnS core/shell *q*-dots, as well as R6G dye. I_0 is the initial fluorescence intensity and *I* is the fluorescence intensity of the sample under continuous excitation for different time intervals.

Figure 4b displays the corresponding emission decay curves of the as-prepared Gd:CIS core and Gd:CIS/ZnS core/shell samples. The decay curves were fitted using a dual-exponential function described by Eq. 2.

$$I(t) = \alpha_1 e^{-t/\tau_1} + \alpha_2 e^{-t/\tau_2} \qquad (2)$$

where $I(t)$ is the emission intensity as a function of time (t) after the excitation pulse, α_1 and α_2 are the weighted coefficients of the decay items, and τ represents the decay lifetime for the dual-exponential items.

The average emission lifetime (<τ>) is calculated by Eq. 3.

$$\langle \tau \rangle = [\alpha_1(\tau_1)^2 + \alpha_2(\tau_2)^2]/[\alpha_1\tau_1 + \alpha_2\tau_2] \qquad (3)$$

Table 1 summarizes the decay lifetimes and the weighted coefficients obtained from the fits for the *q*-dots. The lifetime measured for the Gd:CIS core was estimated to be 449 ns and that for the Gd:CIS/ZnS core/shell is 470 ns. According to previous investigations, the long lifetime (τ_1) attributed to the intrinsic recombination (i.e., donor–acceptor pair transition), and the shorter one (τ_2) was ascribed to surface defect states, such as vacancies and dangling bonds.[9,29-31] Therefore, a possible explanation for the elongated lifetimes of the core/shell samples is that overcoating with ZnS shells on Gd:CIS cores reduced the contribution from the short decay (τ_2) associated with surface-related nonradiative centers. This also suggests the formation of Gd:CIS/ZnS core/shell *q*-dots.

In order to investigate the photostability of the Gd:CIS/ZnS core/shell *q*-dots, the relative PL intensity was monitored after continuous irradiation of the structures with a 450 W xenon lamp at 430 nm. Figure 4c shows the relative fluorescence intensity of R6G dye, the as-prepared Gd:CIS core *q*-dots, and the Gd:CIS/ZnS core/shell *q*-dots. It can be seen that the fluorescence of R6G quickly decreased within 10 s under continuous excitation, but no obvious quenching of the core and core/shell *q*-dots is observed after continuous light exposure for 5 min. Figure 4c clearly illustrates that the Gd:CIS core *q*-dots are more photostable than the R6G dye and that they retained approximately 60% of the original PL intensity after 10 min of light irradiation. More importantly, the Gd:CIS/ZnS core/shell *q*-dots exhibit superior photostability as compared to the as-prepared Gd:CIS core *q*-dots. The fluorescence intensity of the Gd:CIS/ZnS core/shell *q*-dots preserved more than 95% of the original intensity after 3 h of excitation. We attribute such remarkable photostability to the protection of the Gd:CIS cores by the ZnS shells. Highly photostable luminescent markers are particularly important in bioimaging applications because it is often desirable to observe markers for extended periods of time against the background of intrinsic cellular emissions.

High-resolution TEM analysis was performed on the formed Gd:CIS core and Gd:CIS/ZnS core/shell *q*-dots, as illustrated in Figure 5. The existence of well-resolved lattice fringes in the high-resolution TEM images indicates the excellent crystalline structures of the as-prepared Gd:CIS *q*-dots (Figure 5a). Figure 5b displays TEM images of Gd:CIS/ZnS *q*-dots with a diameter of ~3.5 nm. Given the small crystal size and thin shell, it is difficult to see the ZnS shell surrounding the Gd:CIS cores by high-resolution TEM. The EDS spectrum (Figure S2a) confirms the presence of Cu, In, Gd, and S in the Gd:CIS *q*-dots, which supports the conclusion that Gd^{3+} ions were incorporated into the $CuInS_2$ host lattice. Meanwhile, the EDS results in Figure S2b confirm the presence of Zn ions in the as-prepared core/shell samples, suggesting the formation of Gd:CIS/ZnS samples. The crystal structures of the Gd:CIS core and Gd:CIS/ZnS core/shell samples is also

elucidated by the XRD patterns shown in Figure S3. The XRD pattern of the Gd:CIS core shows three main peaks at 27.9, 45.8, and 54.1, which can be indexed as the (112), (024), and (132) crystallographic planes, respectively, of the chalcopyrite structure. With an overcoating of ZnS shell, the three major peaks shifted to larger angles relative to those of pure $CuInS_2$, suggesting that the crystal structure of the Gd:CIS *q*-dots was slightly changed by Zn diffusion. These results are consistent with the PL measurements.

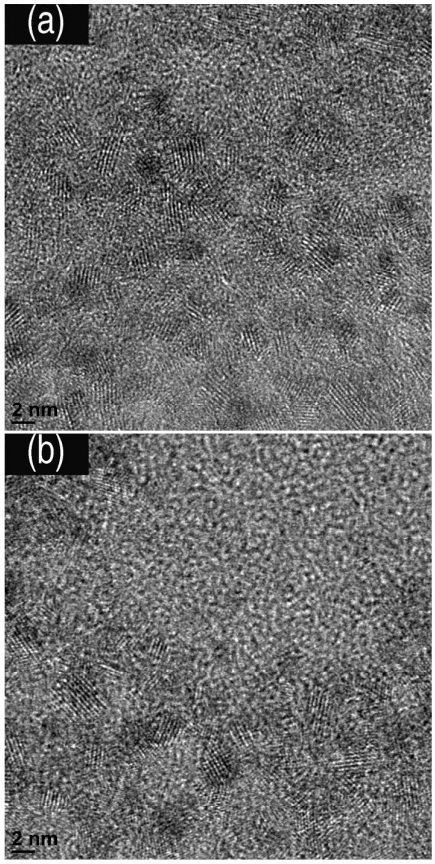

Figure 5. A typical high-resolution TEM image of the (a) as-prepared Gd:CIS core and (b) Gd:CIS/ZnS core/shell *q*-dots.

3.4 EPR measurement and MR imaging evaluation of Gd:CIS/ZnS core/shell *q*-dots

EPR was useful for investigating the local environment of Gd^{3+} dopants inside the host matrix because the spin quantum number of Gd^{3+} is sensitive to changes of its coordination environment. The EPR spectra of the Gd^{3+} centers in the host matrix are described by the following spin Hamiltonian:[32]

$$\hat{H} = g\mu_B \vec{B} \bullet \vec{S} + \alpha\left[S_Z^2 - \frac{1}{3}(S(S+1))\right] + \beta\left[S_X^2 - S_Y^2\right] \qquad (4)$$

where μ_B is the Bohr magneton, $\vec{B}$ is the applied magnetic field, *g* is the electronic *g* factor (assumed to be isotropic), *S* and S_i are the spin operators in the laboratory and zero-field frames, respectively, and α and β are the axial and non-axial zero-field splitting parameters, respectively. The first term describes the Zeeman splitting, the second term describes the axial zero-field splitting, and the third term accounts for the electron-nuclear magnetic hyperfine coupling (^{157}Gd nucleus, $I = 7/2$).

To evaluate the local environment of Gd^{3+} in the Gd:CIS/ZnS *q*-dots, we carried out the synthesis with different starting concentrations of Gd^{3+} precursors and probed the samples by EPR spectroscopy at room temperature (300 K). Figure 6 displays the EPR spectra of a series of Gd:CIS/ZnS *q*-dots prepared at ratios of Cu:Gd, ranging from 1:0 to 1:10. The intensity and peak-to-peak linewidth of the EPR signal was found to vary depending on the Gd^{3+} concentration. The as-prepared sample without Gd^{3+} dopant, S_1, showed no EPR signal. The EPR spectrum of sample S_2 displays a weak, partially resolved signal, whereas the EPR spectrum of sample S_3 exhibits a well-resolved and strong EPR signal. This strong signal originates from the interaction between the electronic spin and the nuclear spin (I = 7/2), indicating electron spin–nuclear spin interactions in isolated Gd^{3+} ion. That means Gd^{3+} dopants were well-separated and uniform distributed inside $CuInS_2$ host-matrix. A similar hyperfine feature is observed for sample S_4, but the EPR intensity is weaker, which is attributed to the isotropic alignment of magnetic moments with increasing gadolinium concentration. With increasing amounts of Gd^{3+} ions added to the Gd:CIS/ZnS *q*-dots, the well-resolved EPR signal disappears in the range of 200–400 mT in the EPR spectra of samples S_5 and S_6; instead, a broad EPR signal appears in the spectra. This change probably arises from clustered or concentrated Gd^{3+} ions with enhanced dipole–dipole interactions. In other words, as the concentration of Gd^{3+} ions increases, Gd^{3+} ions are easily affected by nearby Gd^{3+} ions. These Gd–Gd interactions cause a reduction of the electron spin–nuclear spin interactions in isolated Gd^{3+} ions. This is likely attributed to a non-uniform Gd^{3+} doping or small nanoclusters of Gd^{3+} formed in Gd:CIS *q*-dots because the nanocrystal is prone to expel the excessive dopants, a

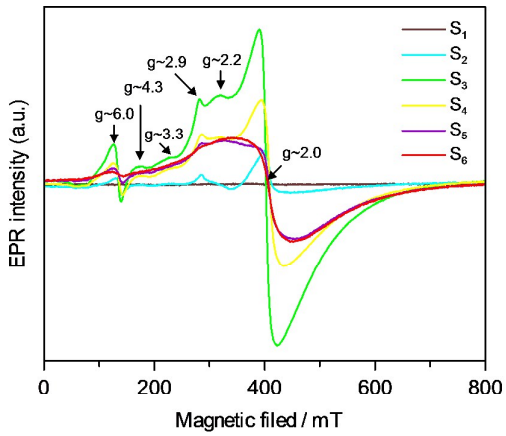

Figure 6. EPR spectra of Gd:CIS/ZnS *q*-dots prepared at different ratios of Cu:Gd. Samples S_1–S_6 represent the feed molar ratios of Cu:Gd of 1:0, 1:0.5, 1:1, 1:2, 1:3, and 1:10, respectively.

process known as ''self-purification'' effect.[33,34] Similar EPR spectra have also been observed in Mn^{2+}-doped QDs, in which hyperfine well-resolved features appeared at low concentrations of Mn^{2+} dopant in QDs, whereas a broad EPR signal was observed for high concentrations of the dopant.[35]

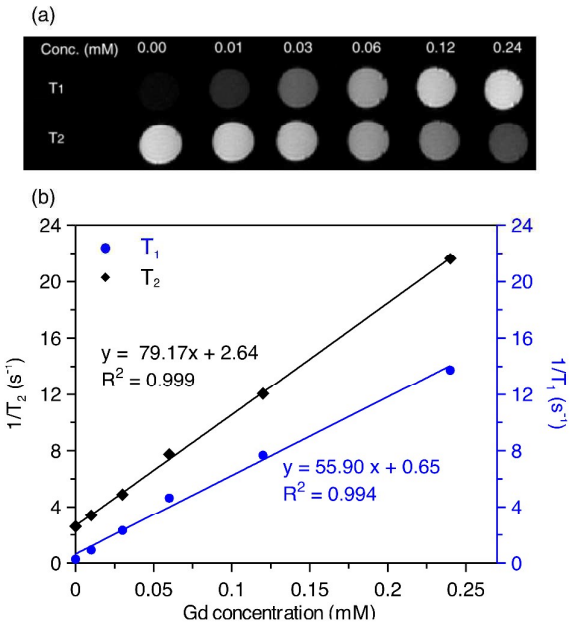

Figure 7. (a) T_1- and T_2-weighted images of phantoms containing various Gd concentrations. (b) Plots of inverse relaxation times ($1/T_1$ and $1/T_2$) versus Gd concentration of the as-synthesized Gd:CIS/ZnS *q*-dots. The slopes correspond to the specific relaxivity values (r_1 and r_2).

To investigate the MR imaging contrasting capability of the Gd:CIS/ZnS *q*-dots, we performed relaxivity measurements and phantom studies on 7T MR scanners, with de-ionized water as a control sample. Typical T_1- and T_2-weighted images of Gd:CIS/ZnS *q*-dot solutions with various concentrations of Gd^{3+} are displayed in Figure 7a. The concentrations of the Gd^{3+} ions were determined by ICP-AES. As shown in Figure 7a, the T_1-weighted images display enhanced contrast as the concentration of Gd^{3+} ions increases, whereas the images show a signal reduction with increasing Gd^{3+} concentration in the T_2-weighted images. Figure 7b illustrates the corresponding transverse relaxation ($1/T_2$) and longitudinal relaxation rates ($1/T_1$) of protons as a function of the concentration of Gd^{3+}. It is observed that the inverse relaxation times vary linearly with increasing Gd^{3+} concentration, and the slope of the plots correspond to the longitudinal (r_1) and transverse (r_2) relaxivities. The specific relaxivities of the Gd:CIS/ZnS *q*-dots, which were determined through linear regression curve fitting of inverse relaxation times plotted against the Gd^{3+} ion concentration, were 55.90 and 79.17 mM^{-1} s^{-1} for r_1 and r_2, respectively. For comparison, we also evaluated the relaxivity of Gd-DTPA (Magnevist, trade name), which is a clinically used T_1-weighted agent, under identical experimental parameters. As shown in Figure S4, the r_1 of Gd-DTPA was determined to be 4.47 mM^{-1} s^{-1}, which is considerably lower than the r_1 values of the Gd:CIS/ZnS *q*-dots. Importantly, the r_1 of the Gd:CIS/ZnS *q*-dots is 12.5 times higher than that of Gd-DTPA. The enhanced r_1 is particularly beneficial for dose reduction and avoiding side effects.[36] Moreover, it is generally known that the enhanced r_1 values, while maintaining small r_2/r_1 ratios of 1–2, are an important parameter for estimating whether a given contrast agent can serve as a highly sensitive positive contrast agent for MR imaging. Owing to the relatively high r_1 value and low r_2/r_1 ratio (1.42) of the Gd:CIS/ZnS *q*-dots, the as-prepared *q*-dots are excellent candidates as positive (T_1-dominated) contrast agents.

4. Conclusions

In summary, we report a facile and efficient microwave-assisted approach for the synthesis of magnetic Gd:CIS *q*-dots within a short reaction time of 10 min. This one-pot synthetic strategy is rapid, simple, and easy to scale up. Through passivation of ZnS shells around Gd:CIS cores, high-quality and robust photostable Gd:CIS/ZnS core/shell *q*-dots with enhanced quantum yields were obtained. To the best of our knowledge, this is the first report that the well-resolved EPR signal of Gd:CIS *q*-dots could be systematically controlled by adjusting the Gd content in the precursor. The *q*-dots featured excellent aqueous dispersibility, robust photostability, and strong fluorescence, as well as a low r_2/r_1 ratio (1.42) and a remarkably high r_1 value (55.90 mM^{-1} s^{-1}), which is significantly higher than those of commercially available T_1 contrast agents. These unique optical/magnetic properties render them promising as a platform for dual-modality imaging (both fluorescence and magnetic resonance) and encourages the development of future clinical applications.

Acknowledgements

This work was supported by Ministry of Science and Technology of the Republic of China under Contract No. 102-2628-M-011-001-MY3 and 104-2119-M-011-001. We thank 7T animal MRI Core Lab of the Neurobiology and Cognitive Science Center, National Taiwan University for technical and facility supports.

Notes and references

‡ Footnotes relating to the main text should appear here. These might include comments relevant to but not central to the matter under discussion, limited experimental and spectral data, and crystallographic data.

(1) V. Bagalkot, L. Zhang, E. L. Nissenbaum, S. Jon, P. W. Kantoff, R. Langer and O. C. Farokhzad, *Nano Lett.,* 2007, **7**, 3065–3070.
(2) T. Jamieson, R. Bakhshi, D. Petrova, R. Pocock, M. Imani and A. M. Seifalian, *Biomaterials,* 2007, **28**, 4717–4732.
(3) P. Zrazhevskiy, M. Sena and X. Gao, *Chem. Soc. Rev.,* 2010, **39**, 4326–4354.
(4) R. Bilan, F. Fleury, I. Nabiev and A. Sukhanova, *Bioconjugate Chem.,* 2015, **26**, 609–624.
(5) D. Deng, Y. Chen, J. Cao, J. Tian, Z. Qian and S. Achilefu, *Chem. Mater.*, 2012, **24**, 3029–3037.
(6) J. S. Niezgoda, E. Yap, J. D. Keene, J. R. McBride and S. J. Rosenthal, *Nano Lett.*, 2014, **14**, 3262–3269.

(7) Z. Pan, I. Mora-Seró, Q. Shen, H. Zhang, Y. Li, K. Zhao, J. Wang, X. Zhong and J. Bisquert, *J. Am. Chem. Soc*., 2014, **136**, 9203–9201.
(8) J. -C. Hus, C. -C.; Huang, K. -L. Ou, N. Lu, F. -D. Mai, J. -K. Chen and J. -Y. Chang, *J. Mater. Chem.,* 2011, **21**, 19257–19266.
(9) C. -Y. Cheng, K. -L. Ou, W. -T. Huang, J. -K. Chen, J. -Y. Chang and C. -H. Yang, *ACS App. Mater. Interfaces*, 2013, **5**, 4389–4400.
(10) C. -C. Chang, J. -K. Chen, C. -P. Chen, C. -H. Yang and J. -Y. Chang, *ACS App. Mater. Interfaces,* 2013, **5**, 11296-11306.
(11) H. He, M. Feng, J. Hu, C. Chen, J. Wang, X. Wang, H. Xu and J. R. Lu, *ACS Appl. Mater. Interfaces,* 2012, **4**, 6362–6370.
(12) S. Liu, J. Hu, H. Zhang and X. Su, *Talanta,* 2012, **101**, 368–373.
(13) W. -W. Xiong, G. -H. Yang, X. -C. Wu and J. -J. Zhu, *ACS Appl. Mater. Interfaces,* 2013, **5**, 8210–8216.
(14) Y. Chen, S. Li, L. Huang and D. Pan, *Nanoscale,* 2014, **6**, 1295–1298.
(15) Y. Chen, S. Li, L. Huang and D. Pan, *Inorg. Chem*., 2013, **52**, 7819–7821.
(16) B. Chen, H. Zhong, W. Zhang, Z. Tan, Y. Li, C. Yu, T. Zhai, Y. Bando, S. Yang and B. Zou, *Adv. Mater*., 2012, **22**, 2081–2088.
(17) M. Uehara, K. Watanabe, Y. Tajiri, H. Nakamura and H. Maeda, *J. Chem. Phys*., 2008, **129**, 134709.
(18) Y. -K. Kim, S. -H. Ahn, K.Chung, Y. -S. Cho, C. -J and Choi, C. -J. *J. Mater. Chem*., 2012, **22**, 1516–1520.
(19) B. K. Meyer, P. Omling, E. Weigel and G. Muller-Vogt, *Phys. Rev. B*, 1992, 46, 15135.
(20) W. Li, J. Liu, K. Sun, H. Dou and K. Tao, *J. Mater. Chem.,* 2010, **20**, 2133–2138.
(21) M. A. H. Muhammed, P. K. Verma, S. K. Pal, A. Retnakumari, M. Koyakutty, S. Nair and T. Pradeep, *Chem. Eur. J.,* 2010, **16**, 10103–10112.
(22) A. Mathew, P. R. Sajanlal and T. Pradeep, *J. Mtaer. Chem*., 2011, **21**, 11205–11212.
(23) T. Zhou, Y. Huang, Z. Cai, F. Luo, C. J. Yang and X. Chen, *Nanoscale*, 2012, **4**, 5312–5315.
(24) J. S. Mohanty, P. L. Xavier, K. Chaudhari, M. S. Bootharaju, N. Goswami, S. K. Pal and T. Pradeep, *Nanoscale*, 2012, **4**, 4255–4262.
(25) Y. Li, Y. Hu, Y. Zhao, G. Shi, L. Deng, Y. Hou and L. Qu, *Adv. Mater.* 2011, **23**, 776–780.
(26) L. L. Li, J. Ji, R. Fei, C. Z. Wang, Q. Lu, J. R. Zhang, L. P. Jiang and J. J. Zhu, *Adv. Funct. Mater,* 2012, **22**, 2971–2979.
(27) L. Tang, R. Ji, X. Li, K. S. Teng and S. P. Lau, *J. Mater. Chem. C*, 2013, **1**, 4908–4915.
(28) X. T. Zheng, A. Ananthanarayanan, K. Q. Luo and P. Chen, *Small*, 2015, **11**, 1620–1636.
(29) H. Zhong, Y. Zhou, M. Ye, Y. He, J. Ye, C. He, C. Yang and Y. Li, *Chem. Mater*., 2008, **20**, 6434–6443.
(30) X. Tang, K. Yu, Q. Xu, E. S. G. Choo, G. K. L. Goh and J. Xue, *J. Mater. Chem*., 2011, 21, 11239–11243.
(31) L. D. Trizio, M. Prato, A. Genovese, A. Casu, M. Povia, R. Simonutti, M. J. P. Alcocer, C. D'Andrea, F. Tassone and L. Manna, *Chem. Mater*., 2012, **24**, 2400–2406.
(32) D. T. Edwards, Z. Ma, T. J. Meade, D. Goldfarb, S. Han and M. S. Sherwin, *Phys. Chem. Chem. Phys.,* 2013, **15**, 11313–11326.
(33) D. J. Norris, A. L. Efros and S. C. Erwin, *Science*, 2008, **319**, 1776–1779.
(34) G. M. Dalpian and J. R. Chelikowsky, *Phys. Rev. Lett*., 2006, **96**, 226802.
(35) A. Nag, S. Sapra, C. Nagamani, A. Sharma, N. Prahan, S. V. Bhat and D. D. Sarma, *Chem. Mater*., 2007, **19**, 3252–3259.